



Subject Areas:

Life sciences–engineering interface

Keywords:

wound healing, finite element method, cell diffusivity, numerical modeling, nonlinear diffusion

Author for correspondence:

Ahmed S. Dalaq

e-mail: ahmed.dalaq@kfupm.edu.sa

Fickian Modelling of Wound Healing: A Spatially Variable Diffusivity with Applications

Ekrem Ekici¹, Fatma Alzamel² and Ahmed S. Dalaq^{1,2}

¹Interdisciplinary Research Center for Biosystems and Machines, King Fahd University of Petroleum and Minerals, Dhahran, 31261, Saudi Arabia

²Department of Bioengineering, King Fahd University of Petroleum and Minerals, Dhahran, 31261, Saudi Arabia

This work presents a simple framework that combines automated edge detection, coordinate extraction, and finite element modeling to capture wound healing kinematics. We use wound images from diabetic and non-diabetic groups and apply edge detection via a Chan–Vese approach together with custom morphological filtering. This yields accurate wound boundaries over 14 days, which form the initial diffusion domain for a Fickian diffusion-based healing model. Simulations performed with a constant diffusion coefficient captured overall healing trends but failed to reproduce the spatial shifts of the wound edges. To address this, we introduced a spatially varying diffusion field implemented through a Poisson-based geometric descriptor and Gaussian modulation. The resulting model effectively captured the evolving wound edge over time and reflected known biological behavior: healthy and nitrate-treated wounds showed stronger diffusivity gradients and higher cell activity, whereas diabetic wounds exhibited flatter diffusion profiles and reduced proliferation. Importantly, the model captured how nitrate treatment improve healing in the diabetic cases.

1. Introduction

Cell diffusion and cell growth (mitotic generation) are primary mechanisms in both analytical and numerical wound healing models [1–3]. The wound edge progressively migrates toward the center (i.e., cell diffusion) and proliferation (i.e., mitotic generation). Consequently, for a given wound size, Fickian diffusion can model the healing process using a diffusion term and logistic mitotic generation one. This model has been extended in numerous studies by incorporating additional mathematical terms to represent chemotactic flux [4], extracellular matrix (ECM) remodeling [5,6], blood vascularization (angiogenesis) [7–9], inflammation and debris clearance [10], and endogenous bioelectric fields [11]. Several numerical approximations have also been proposed to model the transport of oxygen and growth factors within the epidermal layer using the finite element method (FEM) [12]. These frameworks have been further developed to include the dermal wound contraction mechanism [9], angiogenesis and wound closure [13,14], and deep surgical wound [15]. To further enhance the model’s capabilities, mechanical and viscoelastic effects on wound closure are incorporated to quantify contraction forces [16,17]. With these mechanistic additions to the Fickian model, the formulation yields either a system of ordinary differential equations (ODEs) or a single partial differential equation (PDE), each containing several phenomenological parameters linked to the corresponding mechanisms. The scarcity of such measurements impedes the adoption of these models, as calibrating even the simple Fickian diffusion model becomes challenging.

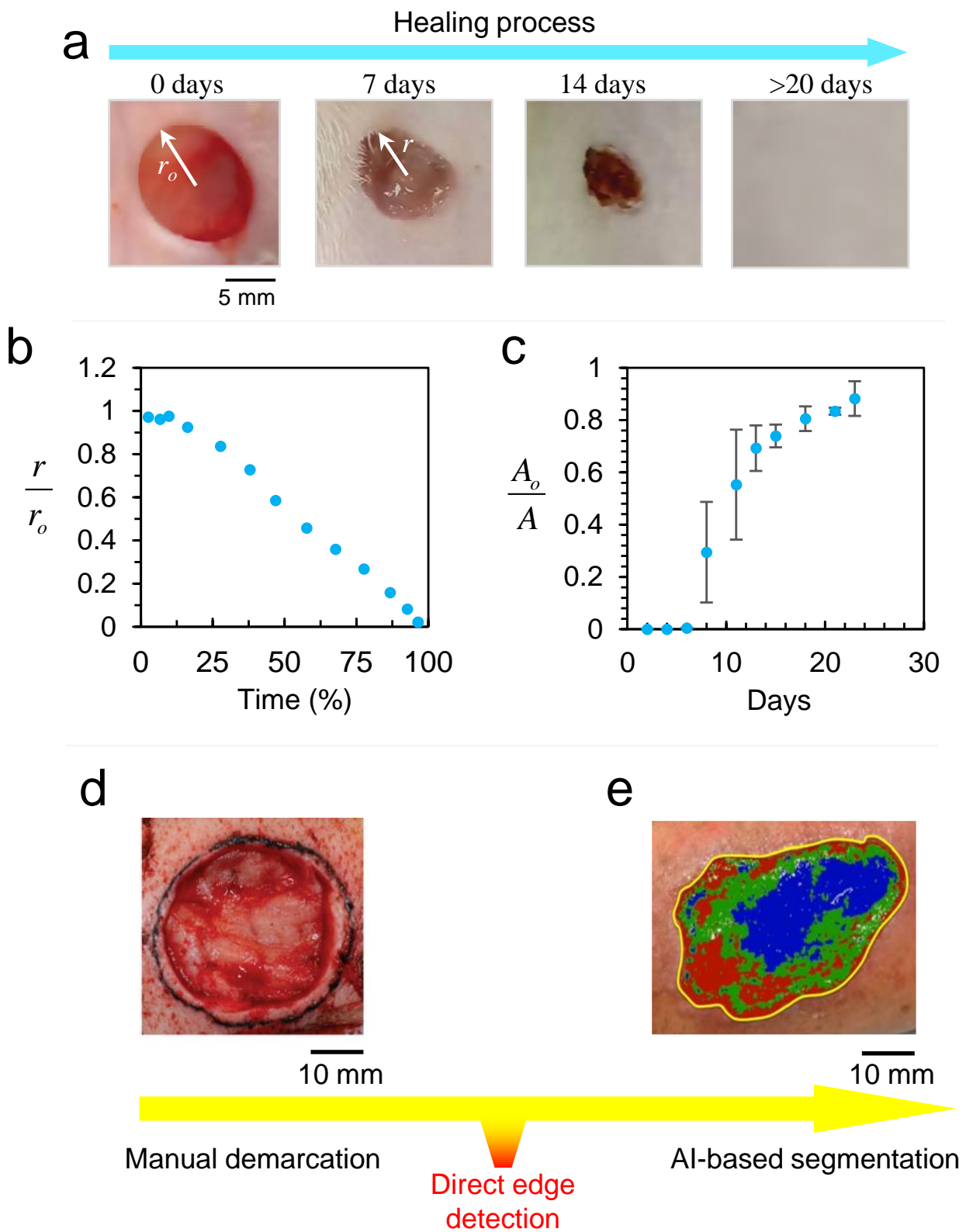


Figure 1. (a) Wound healing progression in a rat animal study over 0–20 days (adapted from [18]). (b) Wound radius over time in an ear wound rabbit case (data are adapted from [1]), showed a tracking ratio suitable for circular wounds. (c) Wound area reduction ratio, ideal for irregular wounds (data are for a square wound in a rat subject, adapted from [19]). (d) Manual demarcation of the wound edge to track healing progress (adapted from [20]). (e) AI-based segmentation applied to capture healing front of the wound (adapted from [21]).

While these mechanistic models add high fidelity to wound modeling and prediction [12,14,22], they must be carefully coupled to the biochemistry and electrical signaling and informed by localized mechanical characterization of the wound. In practice, this entails wound exudate sampling, tissue biopsy, real-time electrical instrumentation, and microindentation of wound sights that current literature largely does not offer. What the literature typically offers are static, top-view wound snapshots (Fig. 1a) taken at discrete time points, with varying resolution and accuracy [19,23–25]. These datasets are neither prevalent nor sufficiently consistent or properly labeled to train large AI (neural network) models for wound-healing prediction, as typical data sets require $\sim 10^3$ images. Nevertheless, AI-based image analysis is effective at handling nonuniform lighting, changes in camera type/resolution, variable snapshot angles, and segmentation of the wound into differently healed regions. In general, available image repositories can be converted into time series of wound-radius or wound-area reduction. Thus, wound kinematics (i.e., wound edge drift) over time can be reported [1] (Fig. 1b).

Given the type of data available in the literature, it may be best practice to use a simple and tractable model such as the basic Fickian model. Recent studies have improved the usage of this simple model by introducing a spatial wound-healing parameter applicable to wounds of arbitrary shape, not limited to ideal circular geometries [26]. In fact, the model is generic and employs a finite element scheme to enable the solution of the PDE for arbitrary two-dimensional shapes and even complex three-dimensional wound morphologies.

Methods for determining the outer boundaries of a wound are highly variable and somewhat inconsistent. These methods range from manual demarcation [20], which inevitably depends on the physician or nurse, to sophisticated AI-based segmentation [21] trained on a myriad of wound images (Fig. 1d–e). The AI approach is indeed powerful; however, neural network training requires large and well-labeled datasets to achieve reliable wound segmentation.

Accounting for the scarcity of wound images available in the literature, we employed a direct edge detection approach using the Chan–Vese active contour model [27,28], combined with several image preconditioning steps. This approach is capable of demarcating the edges of any given wound image without the need for pretraining or extensive fine-tuning of parameters. That is an intermediate method between manual demarcation and AI-based segmentation, as depicted by the “Direct edge detection” mark on the increasing sophistication arrow (Fig. 1d,e). We used the data generated from this approach to calibrate the generic Fickian model for arbitrary wound boundaries and shapes, thereby providing representative combinations of the diffusion coefficient, D , and the rate of mitotic generation, s , for diabetic and non-diabetic cases under different conditions. This enabled direct prediction of healing time, informed by a sequence of wound snapshots for a specific patient or medication [29]. Furthermore, we proposed representing the diffusion coefficient, D , as a spatially varying function to better capture the anisotropic real-time contraction of wound boundaries.

In Sec. 2, we introduce the wound images being considered with implemented image segmentation procedure. Then we use extract coordinates of the wound edges by performing automatic coordinate extraction as explained in Sec. 3. We then use these geometries for modeling healing dynamics with constant diffusion coefficient over the domain (Sec. 4). This then motivates us to define spatially varying diffusion coefficient (Sec. 5). Having combined all the workflow, we demonstrate the capability of our numerical framework for different wounds in Sec. 6. We finally summarize the findings of the paper in Sec. 7 and present the methods in Sec. 8.

2. Segmentation of wound images

A dataset of circular wound images was retrieved from a wound healing study on rate models [25]. In this study, they tracked the kinematics of the wound during healing over a span of 14 days, as shown in Fig. 2a. Reported data included snapshots of diabetic and non-diabetic rat models, with and without the administration of pharmacological treatments (e.g., STZ, NaCl and nitrates). Those images served as valuable inputs, providing consistent data on wound shape and size during closure (i.e., healing). Images are captured consistently with fixed camera conditions and scale.

First, we preprocess the wound images to enhance visual contrast and ensure consistent input quality for segmentation (Fig. 2b). The RGB base image is converted to the CIE L*a*b* color space [30] to decouple luminance from chromaticity, allowing better isolation the wound regions according to color characteristics. Next, the lightness (L^*) and red–green (a^*) components are normalized to a 0–1 scale using intensity rescaling to emphasize darker and redder areas corresponding to wound (see Sec. 8).

We apply morphological operations, including opening (erosion followed by dilation), closing (dilation followed by erosion), and hole filling, to remove small artifacts, smooth irregular boundaries, and maintain region continuity. Fresh wounds, particularly around days 0–3, are typically moist and exhibit low color contrast with the surrounding skin; therefore, such morphological smoothing is necessary for precise edge detection (Fig. 2c) [31] (See Sec. 8).

Next, we use the Chan–Vese active contour model [28], which evolves an initial contour derived from the thresholded wound seed toward the true wound boundaries. This approach does not rely on edge gradients and is therefore effective for segmenting low-contrast, irregular wounds. The contour evolution process produces a binary wound mask (Fig. 2d), representing a smooth, closed boundary that accurately demarcates the wound area. The resulting binary masks are further refined through Gaussian smoothing and area filtering to retain the largest connected region and ensure a clean, precise

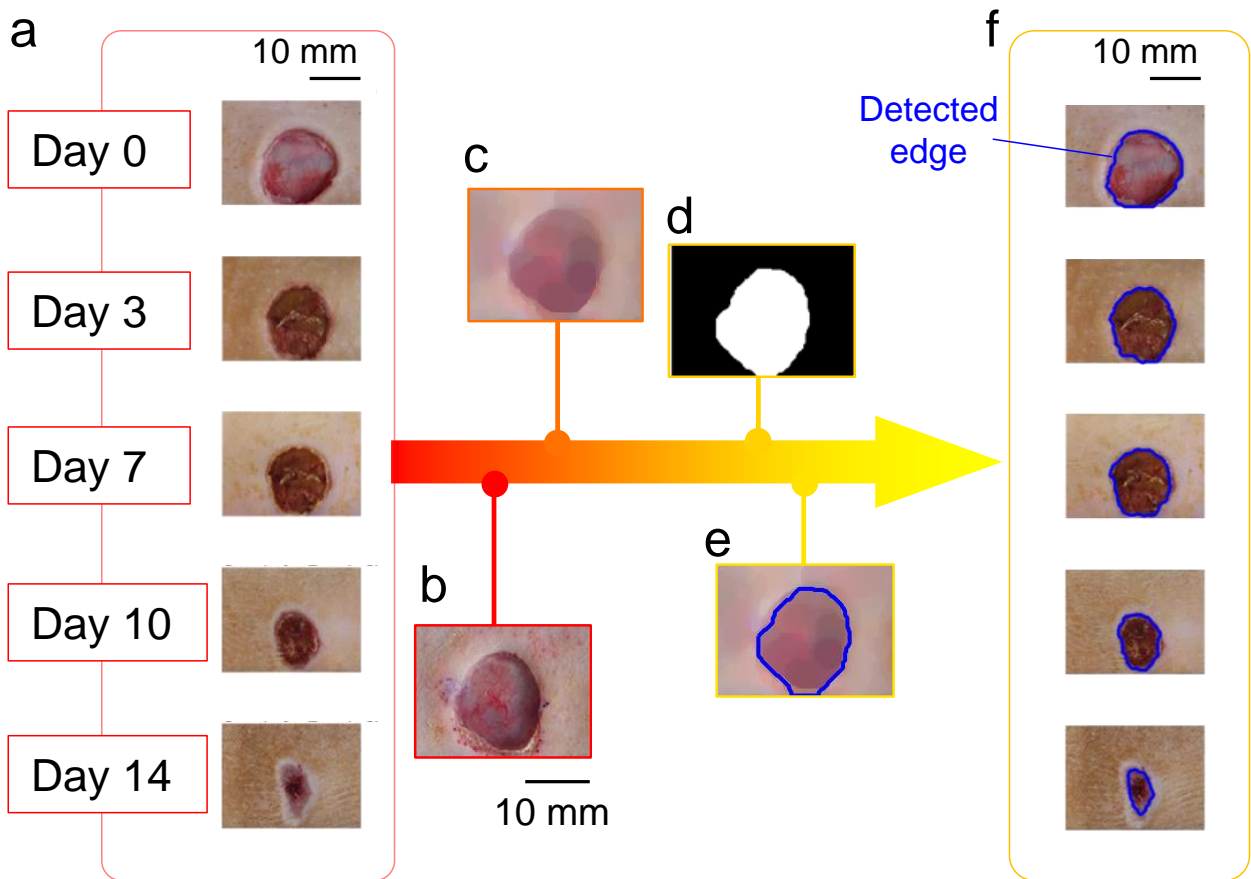


Figure 2. Image preprocessing and segmentation workflow for quantifying wound areas. (a) Sequential wound images collected at Days 0, 3, 7, 10, and 14. (b) Representative wound region isolated for processing. (c) Image conditioning and preprocessing via smoothing. (d) Binary wound mask. (e) Final wound boundaries (outlined in blue) are superimposed on the original image. (f) Overlays of segmented wound boundaries across all days.

wound mask. Finally, we process these challenging images using hole-filling, convex hull [32], and erosion operations (Fig. 2e). The resulting segmentation outcomes for each wound case across all days are shown in Fig. 2f.

We applied the above framework using the same morphological smoothing parameters and weights to all images [25]. The outcome is a series of high-quality image matrices showing wounds treated with various agents and their evolution over different days (Fig. 3). The first column serves as the control, representing a healthy rat model with untreated wounds. The second column shows the wound for a healthy rat model treated with nitrate, a potent promoter of angiogenesis and improved blood circulation [25,33]. The remaining four columns correspond to the diabetic rat model (shaded in orange), induced via streptozotocin (STZ). The last three columns of the image matrix were treated with NaCl, rhEGF, and nitrate, respectively. NaCl flushes out debris, reduces bacterial contamination, and maintains a moist wound environment, while rhEGF, an epidermal growth factor, enhances reepithelialization [34,35]. All wounds progressively shrink over time, accompanied by evident changes in coloration. Around the third day, most wounds turned reddish-brown, indicative of new tissue (granulation) formation [36]. Qualitatively, we observed that the smallest wound outline among the diabetic cases (i.e., STZ-induced) was achieved in the rhEGF-treated group on day 14 (Fig. 3). Among all cases, the nitrate-treated healthy control exhibited the smallest wound outline overall at day 14.

3. Automatic coordinate extraction

Now that we have automatically detected the wound edges for each image in a given healing series, we extract the corresponding coordinates (x, y) of the wound boundaries across different days. Fig. 4a shows three selected cases for demonstration: STZ with nitrate (diabetic), STZ only (diabetic control), and STZ with NaCl (diabetic treated with sodium chloride), shown for the first and last recorded days (day 0 and day 14). Below each case, we present the corresponding wound-edge coordinates from days 0 to 14 on a centimeter scale, with contour colors ranging from yellow to dark red to indicate progressive wound closure (Fig. 4b).

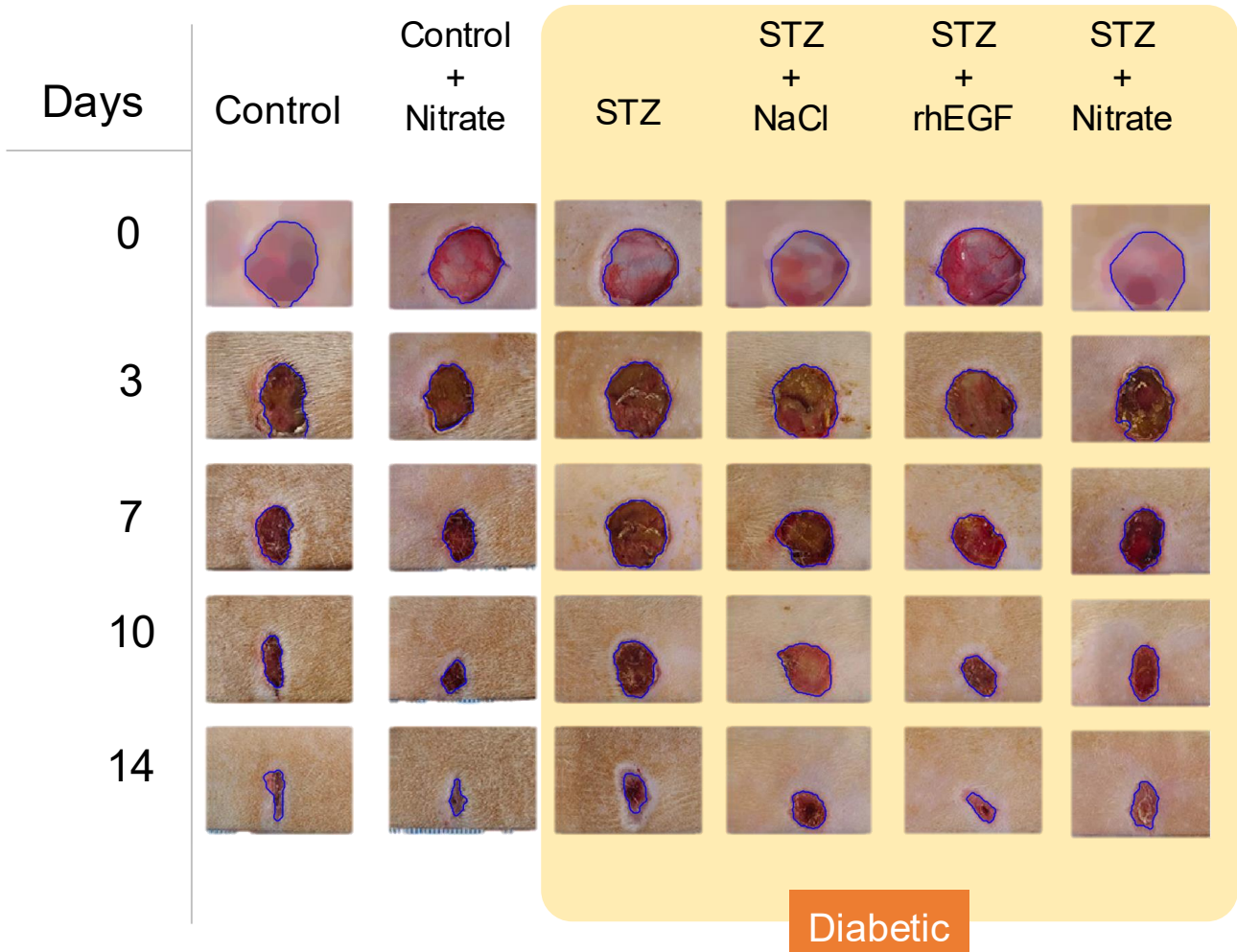


Figure 3. Segmentation results showing extracted wound boundaries across all experimental groups. The raw data is adopted from [25].

These precise wound coordinates are essential for defining the initial wound outline for our FEM (Sec. 8). The remaining coordinate sets are used to extract wound kinematics and quantify wound area reduction over time for comparison with our FEM results (Sec. 8.2).

For each wound dataset corresponding to different healing days, we organize the extracted edge coordinates using a nearest-neighbor algorithm [37], where neighboring points are connected in sequence to form a smooth and continuous wound boundary without any overlaps or edge crossings. The ordered coordinates are then used to reconstruct the wound surface, from which we generate the initial 2D wound geometry and its corresponding mesh for FEM simulations.

4. Using a constant diffusivity field

In this section, we present the numerical estimations of healing kinematics for a simple starting case: the control group (see Fig. 3). The earlier steps allowed us to obtain accurate wound boundaries for each day (0–14). However, the FEM simulation results do not exhibit a sharp wound-edge closure like in the actual experiments, instead, FEM produce a diffuse boundary characterized by a rapid spatial change in cell density, ϕ along wound rim (Fig. 5a). Following previous studies [1,26,38], a cell density threshold of $\phi = 0.8$ may be considered as a healed state and is therefore used to define the wound edge. Mathematically, we can divide the domain into healed and non-healed regions using the following expression:

$$\phi_h(x, y, t) = \begin{cases} 1.0, & \text{if } \phi(x, y, t) \geq 0.8, \\ 0.0, & \text{otherwise,} \end{cases} \quad (4.1)$$

where the subscript h denotes the healed state at each time increment, t . The Eq. (4.1) provides a simple binary division of the domain into healed ($\phi_h = 1$) and non-healed ($\phi_h = 0$) regions (Fig. 5b).

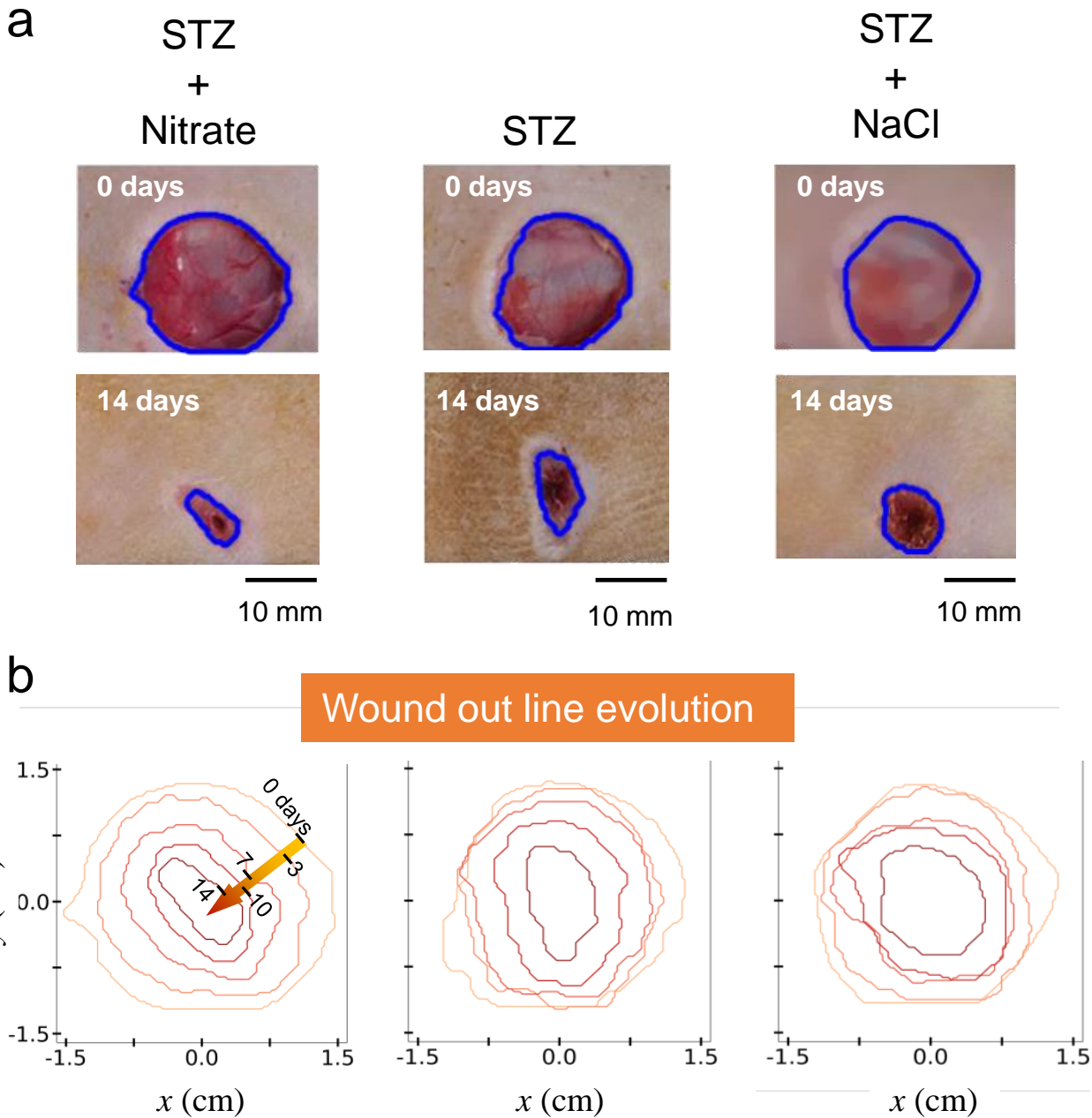


Figure 4. The (a) edge detection for wound image segmentation and (b) extracted coordinates of healing edges for 0, 3, 7, 10 and 14 days.

Based on this domain partitioning into healed (dark red) and non-healed (off-white) regions (Fig. 4.1b), we can estimate the healed area relative to the unhealed area as the ratio $A_i/A(t)$, where A_i is the initial wound area (cm^2) and $A(t)$ is the healed wound area at each time increment. The healed area can be computed incrementally for each day as: $A(t) = \int \phi_h(t) dx$.

We also report the non-dimensional spatial healing metric that represents the overall mean cell density over the wound domain [26]:

$$\beta(t) = \frac{\int \phi(t) dV}{\int dV} \approx \frac{A(t)}{A_i}. \quad (4.2)$$

This metric has the advantage of capturing the overall healing level across the entire domain. Relying on ϕ alone may not adequately represent global healing, since certain regions of the wound may have reached $\phi \geq 0.8$, while large portions

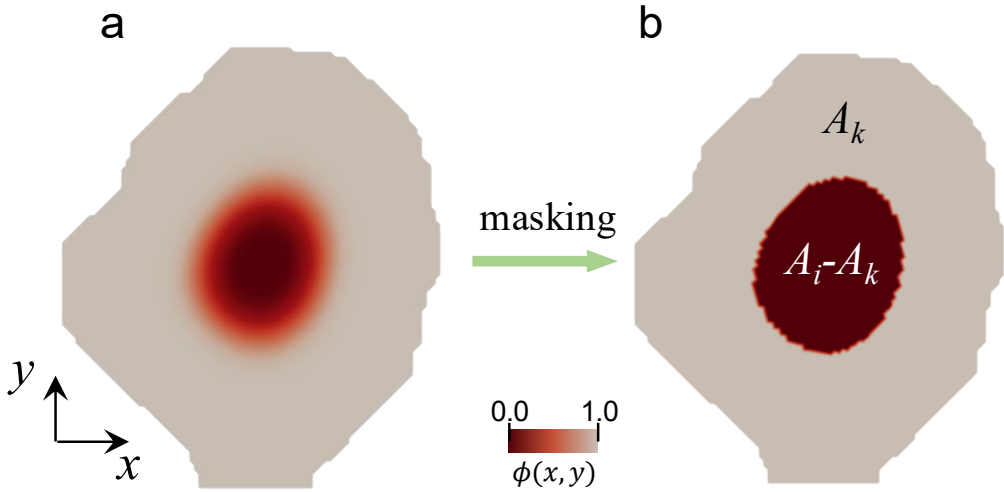


Figure 5. Visualization for Eq. (4.1). The solution vector (a) before and (b) after the masking process where A_i is the initial wound area and A_k is the healed area at k th day.

remain at $\phi \ll 0.8$. The metric β addresses this shortcoming and provides a more comprehensive measure of healing across the entire domain.

During healing process, β asymptotically approaches to 1.0, as $t \rightarrow \infty$. Thus, the FEM solver was terminated when the total healing time, t_h reach 14 days (336 hours).

At this stage, the FEM solver accepts the initial wound boundary obtained from automatic edge detection, along with diffusion coefficient \mathbf{D} , and the mitotic generation rate s . Then it outputs the wound kinematics (i.e., $\phi(x, y, t)$ contours), the post-processed area ratio $A_i/A(t)$, the healing metric $\beta(t)$, and the total healing time t_h . As a first test of the complete framework, we considered the control case (Fig. 6a). The experimental wound boundaries, shown as blue outlines, were first stored. A constant diffusion coefficient of $\mathbf{D} = 8 \times 10^{-5} \text{ cm}^2/\text{h}$ (Fig. 6b) was assigned, which is representative of the diffusion coefficient of the natural wound [39].

Next, we meshed and ran the FEM for the initial wound geometry, corresponding to the outline at day 0. The deviation between the experimental healing duration, $t_{h,e} = 14$ days, and that predicted by the FEM simulation was defined as a loss function, \mathcal{J} , which we minimized by varying only the parameter s . The FEM solver was thus placed in an optimization loop, terminating when the spatial healing parameter approached $\beta \approx 0.99$ (termination criterion). This optimization problem is expressed mathematically as:

$$\begin{aligned} \min \quad & \mathcal{J} = (t_h(\mathbf{D}, s) - t_{h,e})^2, \\ \text{subject to} \quad & \begin{cases} 0.01 \leq s \leq 0.1, \\ \mathbf{D} = 8 \times 10^{-5}, \\ \beta = 0.99. \end{cases} \end{aligned} \quad (4.3)$$

The outcome of the optimization loop yielded a value of $s = 1/30 \text{ h}^{-1}$ (Eq. (4.3)). The resulting wound-kinematic contours, $\phi(x, y, t)$, are shown alongside the actual wound snapshots in Fig. 6a. The corresponding wound area reduction, $A(t)$, and the overall spatial healing metric, $\beta(t)$, are presented in Fig. 6c and Fig. 6d, respectively. The kinematics in Fig. 6a over the first five days show moderate agreement with experimental observations. Spatial deviations are evident along the lateral directions, where the actual wound heals faster laterally, resulting in a narrower and more elongated wound boundary over successive days. Conversely, the calibrated simulation exhibits a uniform contraction of the boundaries toward the center, with the edges drifting inward equally in all directions. As a result, the overall shape of the wound contour is preserved but scaled down isotropically.

When comparing the model-predicted $A(t)$ with the corresponding measurements from the actual wound outlines, the model deviates from the experimental wound area by approximately 30% (Fig. 6c). In terms of the healing metric β , the maximum deviation is reduced to about 9%.

These deviations, both quantitative and spatial, for $A(t)$ and β , are considerable under the adopted approach in Eq. (4.3). The kinematic deviation observed in Fig. 6a strongly depends on how \mathbf{D} is actually distributed across the wound. Therefore, achieving better agreement requires further refinement.

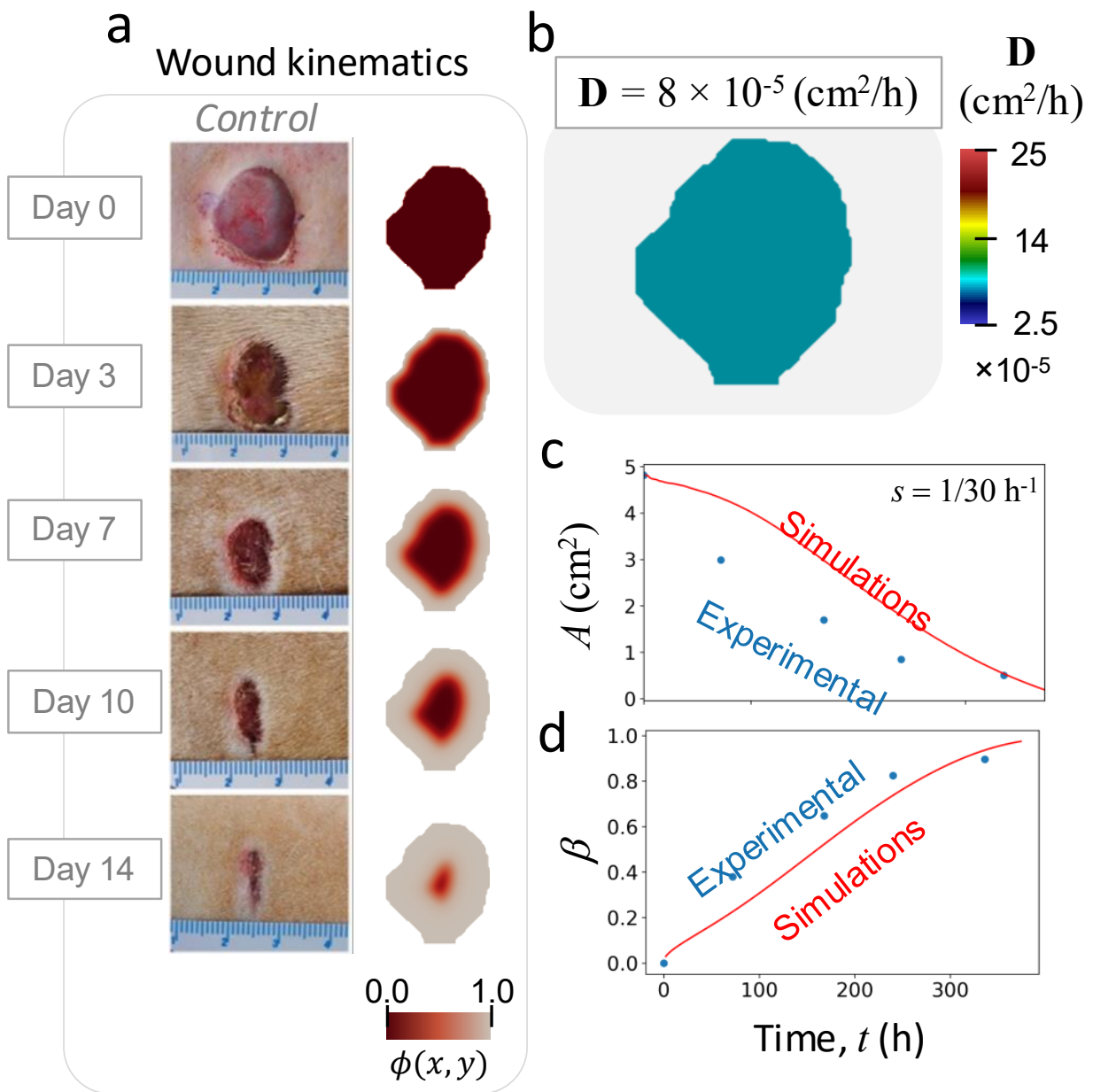


Figure 6. The (a) healing contours for different days (b) for a fixed diffusion coefficient for the control case. The comparison between numerical and experimental results for (c) area ratios and (d) β .

5. Introducing spatially varying diffusivity field

Within continuum wound-healing models such as this one, a radially varying diffusion coefficient has been employed to better capture spatial variations in the extracellular matrix and chemical fields, which in turn influence cell motility [40]. Re-epithelialization is also driven by chemotactic gradients [41], which can be represented through a spatially varying $D(x, y)$ [40,42]. As such, we address the spatial deviation in the wound-healing kinematics by introducing a spatially varying diffusion coefficient, D . In particular, we vary the diffusion profile using a Gaussian function defined by three parameters: the diffusion coefficient at the edge, D_e ; the diffusion coefficient at the center, D_c ; and the spread parameter, σ , which controls the transition of D from the center to the edge.

For any given wound geometry, we first solve a Poisson equation, $-\nabla^2\psi = 1$, with zero boundary conditions along the wound edge (see Sec. 8). The solution is then normalized by its maximum value to obtain $\psi_N = \psi / \max(\psi)$. This normalized field provides a smooth spatial distribution that decreases from the wound center to the edges, where $\psi = 0$. For a given σ , we then write:

$$\mathbf{D} = D_e - (D_e - D_c) \frac{\exp\left[-\frac{(1-\psi_N)^2}{2\sigma^2}\right] - \exp\left[-\frac{1}{2\sigma^2}\right]}{1 - \exp\left[-\frac{1}{2\sigma^2}\right]}. \quad (5.1)$$

This diffusion coefficient field is then used in Fickian diffusion model (Eq. (8.3) in Sec. 8) to perform the healing simulations for different cases (Fig. 3). The spatially varying diffusion coefficients are illustrated in Fig. 7, where \mathbf{D} s are highest near the wound rim and gradually decreases toward the center, reflecting the keratinocyte- and fibroblast-rich periphery and the disorganized extracellular matrix (ECM) at the wound center [43,44]. The parameter σ controls the spatial gradient of \mathbf{D} , ranging from $\sigma = 0$ to $\sigma = 1$, which corresponds to a sharp spike (Dirac delta-like function) to a nearly uniform $\mathbf{D}(x, y)$ distribution. Fig. 7b–d illustrate the effect of increasing σ . For all simulations, we set $D_e = 25 \times 10^{-5}$ and $D_c = 2.5 \times 10^{-5} \text{ cm}^2/\text{h}$ for the wound edge and center, respectively. These \mathbf{D} values fall within biologically plausible ranges [45], namely $10^1\text{--}10^3 \mu\text{m}^2/\text{h}$, which correspond to $10^{-7}\text{--}10^{-5} \text{ cm}^2/\text{h}$.

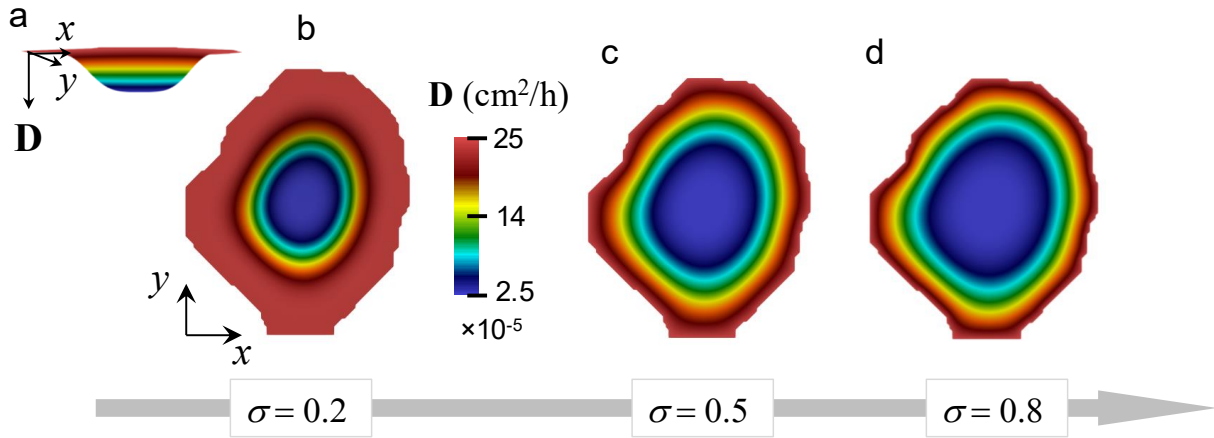


Figure 7. Various diffusivity fields for (a), (b) $\sigma = 0.2$, (c) $\sigma = 0.5$ and (d) $\sigma = 0.8$.

6. Applying spatially varying $\mathbf{D}(x, y)$

Here, we apply the spatially varying diffusion coefficient \mathbf{D} , where the FEM takes the initial wound outline along with $(s, \mathbf{D}(\sigma))$ as inputs and outputs the wound kinematics $\phi(x, y, t)$, the wound area $A(t)$, and the healing metric $\beta(t)$ and the total healing time t_h at $\beta \approx 0.99$. We improve the calibration approach by ensuring that the total wound area during contraction is accurately accounted for by computing its deviation from the experimental measurements. More precisely, we tune the spread parameter, σ and the mitotic generation rate, s so that the numerical results fit the experimental data with an $R^2 \approx 95.0\%$, at each time increment, t . This optimization problem reads:

$$\min \quad \left(R^2(s, \sigma) - 0.95 \right)^2 = \left(0.05 - \frac{\sum_{t=1}^{t_h} (A_{\text{FEM},t}(s, \sigma) - \hat{A}_{\text{exp},t})^2}{\sum_{t=1}^{t_h} (A_{\text{FEM},t}(s, \sigma) - \bar{A}_{\text{exp},t})^2} \right),$$

subject to

$$\begin{cases} 0.01 \leq s \leq 0.1, \\ 0.00 < \sigma < 1.0, \\ D_e = 25 \times 10^{-5}, \\ D_c = 2.5 \times 10^{-5}, \end{cases} \quad (6.1)$$

where $A_{\text{FEM},t}$ and $\hat{A}_{\text{exp},t}$ denote the wound areas for numerical computations and experiments at a given t , respectively and $\bar{A}_{\text{exp},t}$ is the mean healed area from the experimental data. To enable pointwise comparison, we interpolated the missing experimental wound area values at each t .

For the same case shown earlier (Fig. 8a), the optimization yielded $(\sigma, s) = (0.65, 1/24 \text{ h}^{-1})$ (Fig. 8b). This set of parameters produced simulation results that closely matched the experimental wound area, as enforced by Eq. (6.1) (Fig. 8c), and also with the spatial healing parameter β (Fig. 8d). A slight deviation of about 15% was observed at $t = 72 \text{ h}$. Overall, the calibrated parameter combination (s, σ) captured the healing behavior and the β trends well. The wound

kinematics, which are the primary motivation of this work, are now better represented with the introduction of **D**. In this case the wound becomes more elongated and exhibits faster healing along the lateral direction (Fig. 8a).

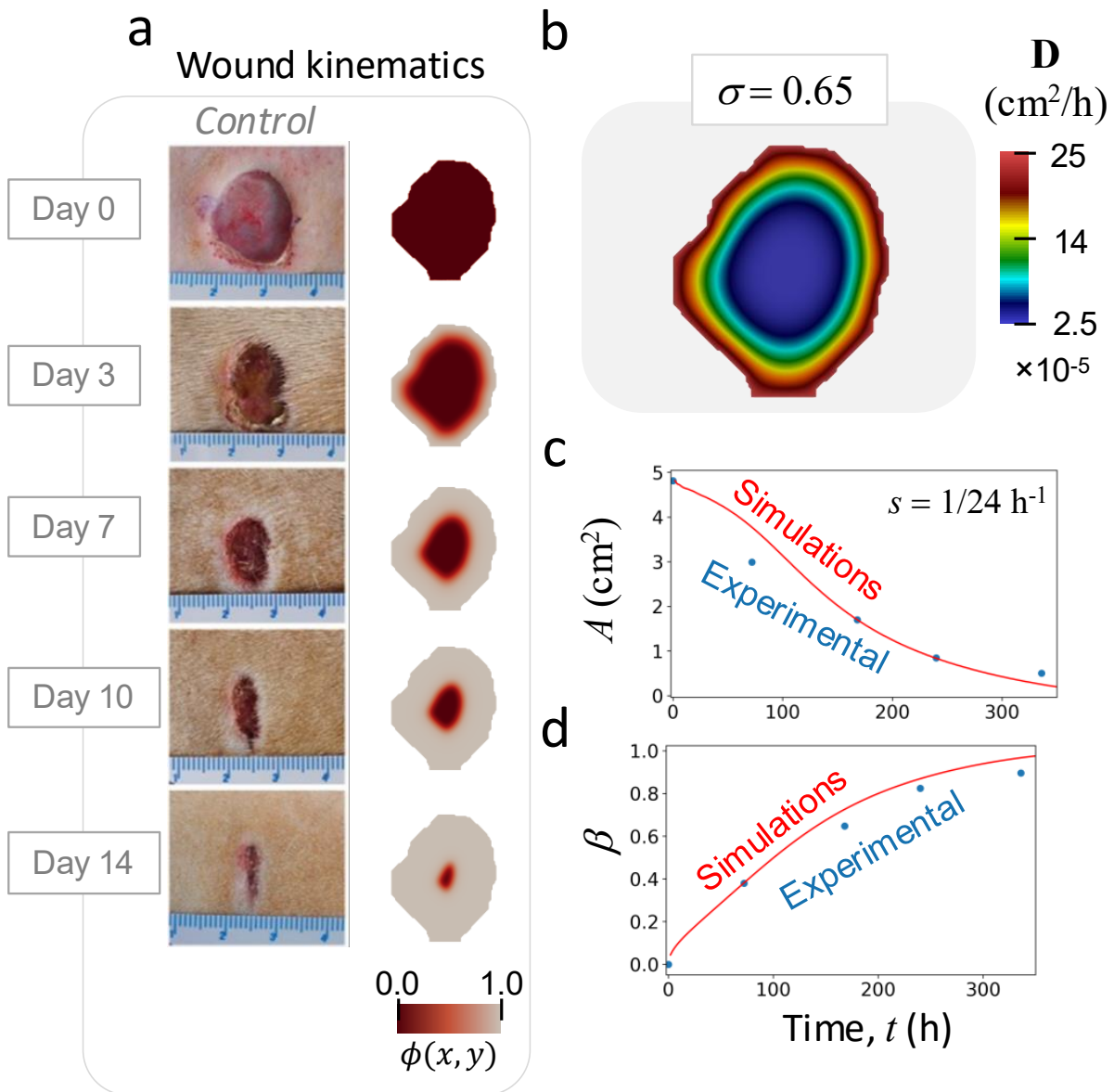


Figure 8. As for Fig. 6 but for the varying diffusion coefficient.

We again apply the spatially varying diffusion coefficient **D** together with the optimization scheme defined in Eq. (6.1) to two diabetic rat-model cases: STZ (Fig. 9a) and STZ+Nitrate (Fig. 10a). For the STZ case, the optimization yielded $(\sigma, s) = (0.90, 1/40 \text{ h}^{-1})$ (Fig. 9b). The introduction of STZ, which induces diabetes in the rat, clearly led to a reduction in the mitotic generation rate by approximately 40%. In terms of wound kinematics, these parameters show good agreement with the experimental wound contours on the left (Fig. 9a), although the actual wound appears slightly more elongated. There is a noticeable deviation in the overall spatial healing parameter β , where the experimental trend resembles a sigmoid curve. Interestingly, the optimization algorithm converged to a high σ value, indicating a flatter spatial distribution of **D**. In other words, there is no sharp contrast in **D**, which may be related to the reduced physiological contrast between the edges of the wound rich in keratinocytes and fibroblasts with strong angiogenic signals and the immature, disorganized ECM in the center of the wound. This healthy contrast is largely absent in the diabetic wound, which is reflected in the very high σ value.

For the STZ case treated with nitrate, the optimization run led to $(\sigma, s) = (0.90, 1/24 \text{ h}^{-1})$ (Fig. 10). Kinematically, the wound closure contours in Fig. 10 show that the simulation successfully captured the oblique wound boundaries

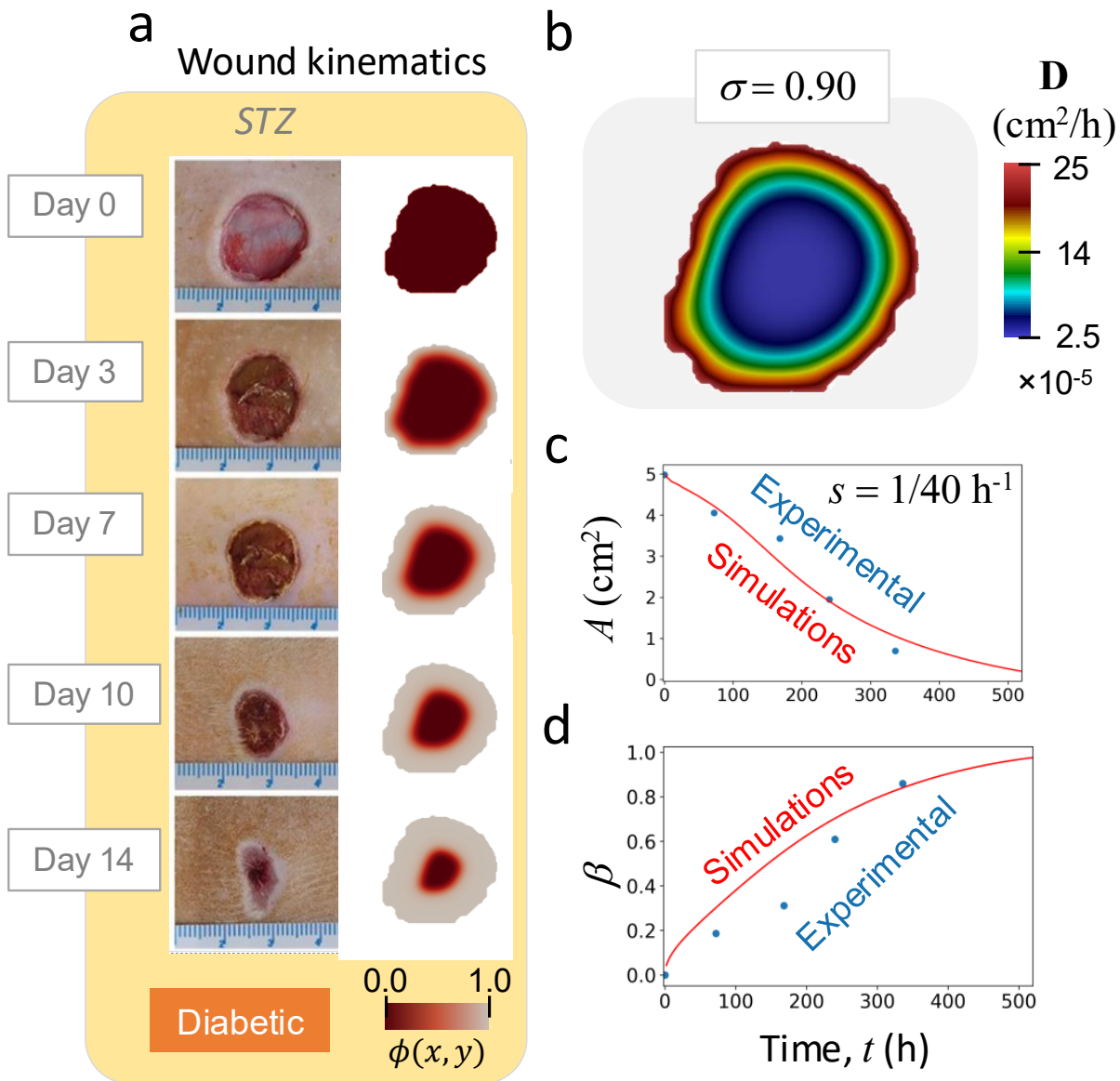


Figure 9. As for Fig. 8 but for the STZ case.

observed at day 14. This mitotic generation s represents an improvement in the mitotic generation rate of approximately 67%, attributable to the addition of nitrates. Similar to the diabetic case without treatment, the optimization did not require a sharply varying spatial diffusivity (i.e., $\sigma = 0.90$), again reflecting the absence of the strong diffusion contrast seen in healthy wounds. STZ appears to be associated with a relatively flat D distribution. Both the $A(t)$ - t and β - t plots agree well with the experimental data (Fig. 10c,d). A similar analysis is carried out for STZ with NaCl (Fig. 3) and further added to Fig. 11.

Fig. 11 compiles the calibrated (σ, s) values as grey and pink bar plots for all cases modeled using the above approach. To the far right, we show the total healing time predicted by the calibrated FEM simulations in hours (dark blue bars), corresponding to each rat-model case. Overall, we extract the following observations:

(i) The control case treated with nitrate possesses the lowest σ value, which reflects physiological realism. A healthy wound, especially when enhanced with nitrate, exhibits a strong contrast in diffusivity D between the highly active wound edges and the center.

(ii) The untreated control case follows, with a σ value about 0.8 times that of the nitrate-treated control. The mitotic generation rate is slightly higher in the untreated case by approximately 4%. The total healing times for both control cases are comparable, around 17 days.

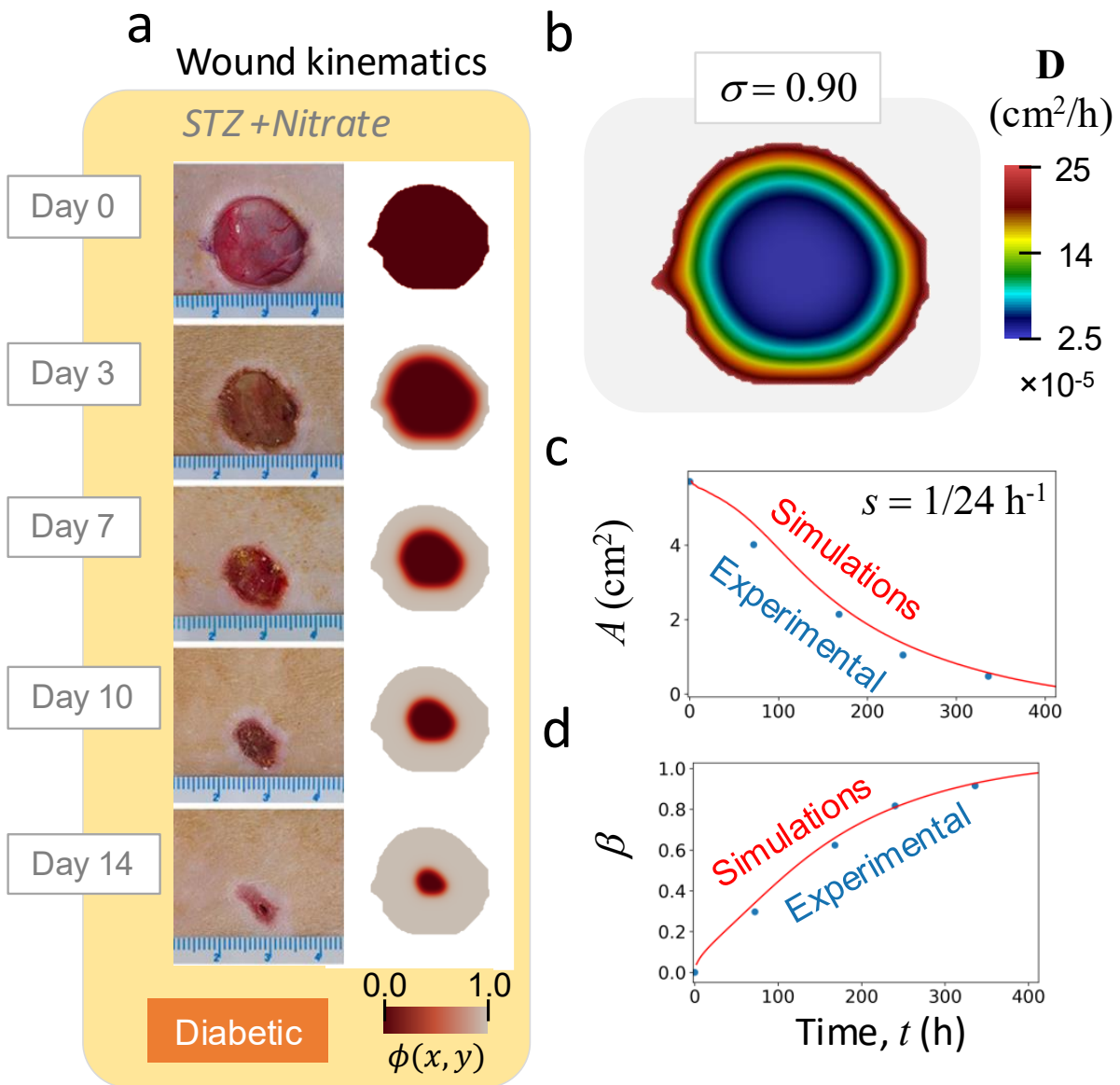


Figure 10. As for Fig. 9 but for the STZ+Nitrate case.

(iii) All diabetic cases consistently yield a flatter spatial distribution \mathbf{D} , indicating the absence of the desired \mathbf{D} contrast between the angiogenically active wound edges and the disorganized ECM and granulation tissue near the center. The mitotic generation rate is notably lower for both STZ cases, and NaCl treatment does not appear to improve the healing process: it neither increases s nor reduces the healing time T_h , with both STZ and STZ+NaCl cases requiring approximately 23 days.

(iv) In contrast, the STZ+Nitrate case shows a significant improvement for quicker healing. The calibrated parameters indicate a substantial increase in s , and the FEM simulation predicts a reduced healing time of 18 days, which is only one day longer than the control case and four days shorter than the other diabetic cases.

7. Conclusion

We developed a numerical framework that integrates image-based wound edge detection, automatic boundary extraction, and a finite element formulation (FEM) for modeling wound healing kinematics. The edge detection scheme captured wound outlines across wound cases with various treatments. Thus, enabled consistent geometric inputs for the numerical model (FEM). By converting experimental wound images into coordinate, we were able to establish a direct link between observed wound closure and continuum-level healing simulations.

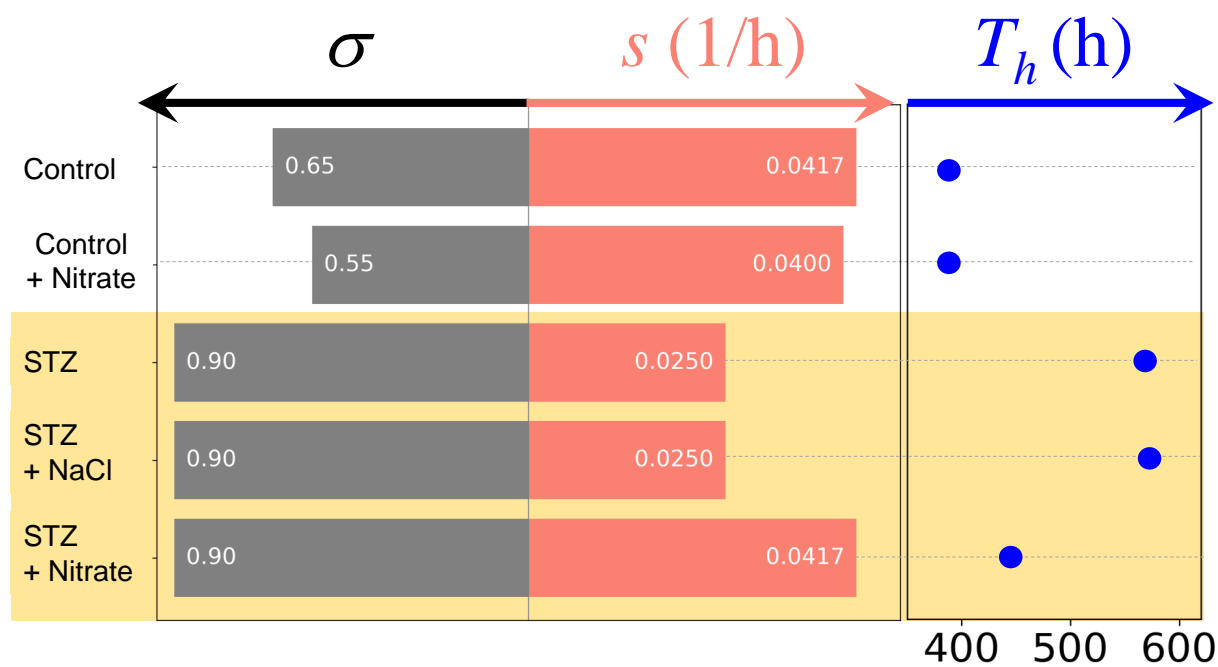


Figure 11. σ values to generate diffusion coefficient fields and s (mitotic generation) of Control, Control+Nitrate, STZ, STZ+NaCl, STZ+Nitrate wound cases. Blue markers show the total healing times for corresponding (σ, s) couples.

At first, using a constant diffusion coefficient initially revealed limitations in capturing experimental kinematics. The simulated wounds contracted isotropically and underestimated the spatial heterogeneity observed in real wounds. Thus motivated us to introduce spatially varying diffusion coefficient $D(x, y)$ which has notably improved the agreement with experiments. We improved the scheme further by fitting the wound area evolution and the healing metric β , consistently yielded parameter sets (D, s) that reflected known biological differences between healthy and diabetic wounds like the active angiogenesis at wound rim and granulation at its center.

The calibrated diffusion and mitotic generation parameters highlighted clear physiological trends. Healthy wounds, especially those treated with nitrate, exhibited strong diffusivity contrast and higher mitotic activity, resulting in faster healing. Conversely, all diabetic cases produced flatter diffusion coefficient fields, $D(x, y)$, and lower cell proliferation rates s . Notably, nitrate treatment partially restored healing performance in diabetic wounds, and so reduce healing time by several days. Overall, the proposed framework provides a quantitative and deterministic tool for linking experimental wound images with continuum healing models, and it offers a simple approach for future predictive simulations and treatment optimization of chronic wounds.

Finally, this work represents an improvement over the iso-line approach adopted in [26], where unique combinations of (D, s) can now be informed by accurate tracking of the wound boundaries, but with one caveat: it requires more wound healing data.

8. Methods

8.1 Morphological Smoothing

We applied morphological smoothing via “opening” and “closing” parameters, particularly through tuning the element size and applying bilateral filtering [46] to reduce noise and illumination irregularities while maintaining boundary sharpness. These parameters were determined for each image set to account for differences in wound texture and illumination and were kept fixed throughout the study. A disk-shaped structuring element was employed to ensure isotropic smoothing along wound boundaries. For example, in day 0 for control wound, a sequence of two consecutive closing operations using a 12-pixel disk followed by a 3-pixel opening effectively restored a continuous rim and filled small discontinuities in the wound center caused by uneven illumination. In comparison, the NaCl-treated wound displayed smoother texture but bright peripheral artifacts therefore applying an opening with a smaller 3-pixel disk before closing with a 5-pixel disk efficiently removed surface noise while reconnecting the boundary. In the rhEGF-treated wound the

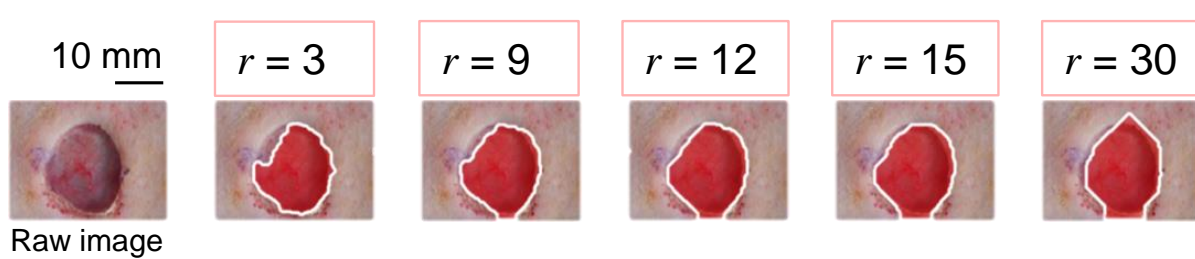


Figure 12. Sensitivity analysis of the structuring element size for morphological preprocessing of the Day 0 Control wound image. The original image is shown alongside masks generated using disk-shaped structuring elements with radii of 3, 9, 12, 15, and 30 pixels.

To demonstrate the influence of structuring element size on boundary formation, a sensitivity test was performed on the day 0 of a control case (Fig. 12). We repeated a sequence of morphological closing and opening operations using disk structuring elements with radii r ranging from 3 to 30 pixels. With a small disk ($r = 3$), the wound edges remained detailed but fragmented, leaving small gaps around the rim uncaptured. As the radius increased to 9 and 12 pixels, the edges became smoother and more connected, producing a natural, continuous wound boundary. For larger radii $r \geq 15$, the mask became overly smoothed and expanded into surrounding skin beyond the true wound edge. An intermediate radius of $r = 12$ provided the most accurate and realistic outline, so this range was selected. The same procedure was applied to the other wound groups with r adjusted accordingly. $r = 12$ struck the best balance for most groups.

8.2 Finite Element Methodology

We solve a Fickian diffusion equation to model the cell dynamics over the healing wound domain. A nonlinear logistic term is included in diffusion equation to capture the mitotic generation [1,26,47,48]:

$$\frac{\partial \phi}{\partial t} = \mathbf{D}[\nabla \cdot (\phi/\phi_0) \nabla \phi] + s\phi(1 - \phi/\phi_0) \quad \text{in } \Omega, \quad (8.1)$$

where ϕ is the cell density, t is the time, ϕ_0 is the unwounded cell density, where \mathbf{D} is a spatially varying scalar field for diffusion coefficient (Sec. 5), and s is the proliferation/mitotic generation rate of the cells in the domain Ω . For Eq. (8.1), the initial condition for all the cases are the identical, the cell density on the wound edge, $\partial\Omega$, is set to one and zero elsewhere, as expressed in Eq. 8.2:

$$\phi(x, y, 0) = \begin{cases} 1.0, & \text{if } x \in \partial\Omega, \\ 0.0, & \text{otherwise.} \end{cases} \quad (8.2)$$

Eq. (8.2) also states the boundary condition of the problem:

$$\phi(x, y, t) = 1.0, \quad \text{if } (x, y) \in \partial\Omega.$$

We set $\phi_0(x, y, t) = 1.0$ (i.e., non-chronic wounds) and set a cartesian grid for solving irregular geometries obtained after segmentation of wound images (Fig. 4). We use finite element method (FEM) to obtain cell activity on spatial wound domain. Thus, we require an FEM discretization of spatial and time derivatives in (8.1) and its boundary conditions. We use degree 1 triangular continuous Galerkin finite elements. We then derive the complete weak formulation of (8.1) in variational form, yielding:

$$\begin{aligned} F(\phi^{n+1}; v) = & \int_{\Omega} [(\phi^{n+1} - \phi^n)v + \Delta t \mathbf{D}(\phi^{n+1}/\phi_0) \nabla \phi^{n+1} \nabla v \\ & - \Delta t s\phi(1 - \phi/\phi_0)v] dx = 0, \end{aligned} \quad (8.3)$$

where v is the test function, Δt is the time step, n is the time level. We set $\Delta t = 2$ h. Since the logistic term ($s\phi(1 - \phi/\phi_0)$) introduces nonlinearity, we implement a nonlinear FEM solver built upon the open-source FEM framework FEniCSx [49–54]. For further details of the weak formulation, timestep convergence and solver implementation, reader is referred to [26].

Acknowledgements. This work was supported by the interdisciplinary Research Center (IRC): Biosystems and Machines at King Fahd University of Petroleum & Minerals (KFUPM). Ekrem Ekici gratefully acknowledges funding for his postgraduate studies from Türkiye's Ministry of National Education.

Authors' Contributions. EE—model generation, numerical data generation, analysis, solver implementation; manuscript writing. FA—image segmentation; manuscript writing. ASD—conceptualization; data analysis and interpretation; manuscript writing.

References

- Sherratt JA, Murray JD. 1990 Models of epidermal wound healing. *Proceedings of the Royal Society of London. Series B: Biological Sciences* **241**, 29–36.
- Fisher RA. 1937 The Wave of Advance of Advantageous Genes. *Annals of Eugenics* **7**, 355–369. _eprint: <https://onlinelibrary.wiley.com/doi/pdf/10.1111/j.1469-1809.1937.tb02153.x>.
- Kolmogorov A. 1937 Étude de l'équation de la diffusion avec croissance de la quantité de matière et son application à un problème biologique. Pages: 1 Publication Title: Moscow Univ. Bull. Ser. Internat. Sect. A Volume: 1.
- Wearing HJ, Sherratt JA. 2000 Keratinocyte growth factor signalling: a mathematical model of dermal–epidermal interaction in epidermal wound healing. *Mathematical Biosciences* **165**, 41–62.
- Schiller M, Javelaud D, Mauviel A. 2004 TGF-Beta-induced SMAD signaling and gene regulation: consequences for extracellular matrix remodeling and wound healing. *Journal of Dermatological Science* **35**, 83–92.
- Menon SN, Flegg JA. 2021 Mathematical Modeling Can Advance Wound Healing Research. *Advances in Wound Care* **10**, 328–344.
- Vermolen FJ, Javierre E. 2012 A finite-element model for healing of cutaneous wounds combining contraction, angiogenesis and closure. *Journal of Mathematical Biology* **65**, 967–996.
- Pettet GJ, Byrne HM, McElwain DLS, Norbury J. 1996 A model of wound-healing angiogenesis in soft tissue. *Mathematical Biosciences* **136**, 35–63.
- Vermolen F, Javierre E. 2010 Computer simulations from a finite-element model for wound contraction and closure. *Journal of Tissue Viability* **19**, 43–53.
- Dunster JL, Byrne HM, King JR. 2014 The Resolution of Inflammation: A Mathematical Model of Neutrophil and Macrophage Interactions. *Bulletin of Mathematical Biology* **76**, 1953–1980.
- Reid B, Zhao M. 2014 The Electrical Response to Injury: Molecular Mechanisms and Wound Healing. *Advances in wound care* **3**, 184–201.
- Vermolen FJ, Adam JA. 2007 A finite element model for epidermal wound healing. In *Computational Science–ICCS 2007: 7th International Conference, Beijing, China, May 27–30, 2007, Proceedings, Part I* 7 pp. 70–77. Springer.
- Flynn C. 2010 Finite element models of wound closure. *Journal of tissue viability* **19**, 137–149.
- Vermolen F, Javierre E. 2012 A finite-element model for healing of cutaneous wounds combining contraction, angiogenesis and closure. *Journal of mathematical biology* **65**, 967–996.
- Valero C, Javierre E, García-Aznar J, Gómez-Benito M. 2014 Nonlinear finite element simulations of injuries with free boundaries: application to surgical wounds. *International journal for numerical methods in biomedical engineering* **30**, 616–633.
- Arciero JC, Mi Q, Branca MF, Hackam DJ, Swigon D. 2011 Continuum model of collective cell migration in wound healing and colony expansion. *Biophysical Journal* **100**, 535–543.
- Pozzi G, Ciarletta P. 2024 Geometric control by active mechanics of epithelial gap closure. *Soft Matter* **20**, 900–908. Publisher: Royal Society of Chemistry.
- Li J, Haiyan C, Lei L, Hao L, Cui Z. 2020 Wound healing activity of neferine in experimental diabetic rats through the inhibition of inflammatory cytokines and nrf-2 pathway. *Artificial Cells, Nanomedicine, and Biotechnology* **48**, 96–106. Publisher: Taylor & Francis _eprint: <https://doi.org/10.1080/21691401.2019.1699814>.
- Giusto G, Vercelli C, Comino F, Caramello V, Tursi M, Gandini M. 2017 A new, easy-to-make pectin-honey hydrogel enhances wound healing in rats. *BMC complementary and alternative medicine* **17**, 1–7.
- Fuchs C, Pham L, Henderson J, Stalnaker KJ, Anderson RR, Tam J. 2021 Multi-faceted enhancement of full-thickness skin wound healing by treatment with autologous micro skin tissue columns. *Scientific Reports* **11**, 1688.
- Barakat-Johnson M, Jones A, Burger M, Leong T, Frotjold A, Randall S, Kim B, Fethney J, Coyer F. 2022 Reshaping wound care: Evaluation of an artificial intelligence app to improve wound assessment and management amid the COVID-19 pandemic. *International Wound Journal* **19**, 1561–1577.
- Vermolen FJ, Javierre E. 2009 A Suite of Continuum Models for Different Aspects in Wound Healing. In Gefen A, editor, *Bioengineering Research of Chronic Wounds: A Multidisciplinary Study Approach*, pp. 127–168. Berlin, Heidelberg: Springer.
- Parella K, Moody K, Wortel D, Colegrave H, Elser JA. 2023 HOXA3 accelerates wound healing in diabetic and aged non-diabetic mammals. *Scientific Reports* **13**, 9923. Publisher: Nature Publishing Group.
- Zimny S, Schatz H, Pfohl M. 2004 The Effects of Ulcer Size on the Wound Radius Reductions and Healing Times in Neuropathic Diabetic Foot Ulcers. *Experimental and Clinical Endocrinology & Diabetes* **112**, 191–194. Publisher: J. A. Barth Verlag in Georg Thieme Verlag KG Stuttgart · New York.

25. Hu X, Xu H, Bu L, Sun J, Deng J, Song K, Wang L, Pang B. 2024 Exploring the wound healing potential of dietary nitrate in diabetic rat model. *Frontiers in Physiology* **15**, 1475375. Published: 20 November 2024.
26. Ekici E, Dalaq AS. 2025 A spatial healing metric for wound healing modeling (accepted, article in press). *Biomechanics and Modeling in Mechanobiology* -.
27. Chan TF, Sandberg BY, Vese LA. 2000 Active contours without edges for vector-valued images. *Journal of Visual Communication and Image Representation* **11**, 130–141.
28. Chan T, Vese L. 1999 An active contour model without edges. In *International conference on scale-space theories in computer vision* pp. 141–151. Springer.
29. Stevenson P, Finnane AR, Soyer HP. 2016 Teledermatology and clinical photography: safeguarding patient privacy and mitigating medico-legal risk. *The Medical Journal of Australia* **204**, 198–200.
30. . 2024 MATLAB version 24.1.0 (R2024a). The MathWorks Inc. Natick, Massachusetts, United States.
31. Serra J. 1983 *Image analysis and mathematical morphology*. Academic Press, Inc.
32. Barber CB, Dobkin DP, Huhdanpaa H. 1996 The quickhull algorithm for convex hulls. *ACM Transactions on Mathematical Software (TOMS)* **22**, 469–483.
33. Lundberg JO, Weitzberg E, Gladwin MT. 2008 The nitrate–nitrite–nitric oxide pathway in physiology and therapeutics. *Nature reviews Drug discovery* **7**, 156–167.
34. Park KH, Han SH, Hong JP, Han SK, Lee DH, Kim BS, Ahn JH, Lee JW. 2018 Topical epidermal growth factor spray for the treatment of chronic diabetic foot ulcers: A phase III multicenter, double-blind, randomized, placebo-controlled trial. *Diabetes research and clinical practice* **142**, 335–344.
35. Wong AYW, Hooi NMF, Yeo BSY, Sultana R, Bee YM, Lee ARYB, Tay SM. 2024 Improving diabetic wound-healing outcomes with topical growth factor therapies. *The Journal of Clinical Endocrinology & Metabolism* **109**, e1642–e1651.
36. Gurtner GC, Werner S, Barrandon Y, Longaker MT. 2008 Wound repair and regeneration. *Nature* **453**, 314–321.
37. de Gomensoro Malheiros M, Walter M. 2015 Simple and efficient approximate nearest neighbor search using spatial sorting. In *2015 28th SIBGRAPI conference on graphics, patterns and images* pp. 180–187. IEEE.
38. Sherratt JA. 1993 Cellular growth control and travelling waves of cancer. *SIAM Journal on Applied Mathematics* **53**, 1713–1730.
39. Sherratt JA, Murray J. 1991 Mathematical analysis of a basic model for epidermal wound healing. *Journal of mathematical biology* **29**, 389–404.
40. Tranquillo RT, Murray J. 1992 Continuum model of fibroblast-driven wound contraction: inflammation-mediation. *Journal of theoretical biology* **158**, 135–172.
41. Wu M, Ben Amar M. 2015 Growth and remodelling for profound circular wounds in skin. *Biomechanics and modeling in mechanobiology* **14**, 357–370.
42. Flegg JA, Menon SN, Maini PK, McElwain DS. 2015 On the mathematical modeling of wound healing angiogenesis in skin as a reaction-transport process. *Frontiers in physiology* **6**, 262.
43. Barker TH, Engler AJ. 2017 The provisional matrix: setting the stage for tissue repair outcomes. *Matrix Biology* **60**, 1–4.
44. Talbott HE, Mascharak S, Griffin M, Wan DC, Longaker MT. 2022 Wound healing, fibroblast heterogeneity, and fibrosis. *Cell stem cell* **29**, 1161–1180.
45. Johnston ST, Shah ET, Chopin LK, Sean McElwain D, Simpson MJ. 2015 Estimating cell diffusivity and cell proliferation rate by interpreting IncuCyte ZOOM™ assay data using the Fisher-Kolmogorov model. *BMC systems biology* **9**, 38.
46. Tomasi C, Manduchi R. 1998 Bilateral filtering for gray and color images. In *Sixth international conference on computer vision (IEEE Cat. No. 98CH36271)* pp. 839–846. IEEE.
47. Tremel A, Cai A, Tirtaatmadja N, Hughes BD, Stevens GW, Landman KA, O'Connor AJ. 2009 Cell migration and proliferation during monolayer formation and wound healing. *Chemical Engineering Science* **64**, 247–253.
48. Maini PK, McElwain DS, Leavesley D. 2004 Travelling waves in a wound healing assay. *Applied Mathematics Letters* **17**, 575–580.
49. Barrata IA, Dean JP, Dokken JS, Habera M, Hale J, Richardson C, Rognes ME, Scroggs MW, Sime N, Wells GN. 2023 DOLFINx: The next generation FEniCS problem solving environment. .
50. Alnæs MS. 2012 UFL: a finite element form language. In *Automated Solution of Differential Equations by the Finite Element Method: The FEniCS Book* , pp. 303–338. Berlin, Heidelberg: Springer.
51. Logg A, Ølgaard KB, Rognes ME, Wells GN. 2012 FFC: the FEniCS form compiler. *Automated Solution of Differential Equations by the Finite Element Method: The FEniCS Book* pp. 227–238.
52. Balay S, Abhyankar S, Adams MF, Brown J, Brune P, Buschelman K, Dalcin L, Dener A, Eijkhout V, Gropp W, Karpeyev D, Kaushik D, Knepley M, May D, McInnes LC, Mills R, Munson T, Rupp K, Sanan P, Smith B, Zampini S, Zhang H, Zhang H. 2020 PETSc Users Manual (Rev. 3.13)..
53. Dalcin LD, Paz RR, Kler PA, Cosimo A. 2011 Parallel distributed computing using Python. *Advances in Water Resources* **34**, 1124–1139.
54. Falgout RD, Yang UM. 2002 hypre: A library of high performance preconditioners. In *International Conference on computational science* pp. 632–641. Springer.